PAPER

Check for updates

Viscotaxis of beating flagella†

Shubham Anand, [ID] Jens Elgeti [ID]* and Gerhard Gompper [ID]*

Many biological microorganisms and artificial microswimmers react to external cues of environmental gradients by changing their swimming directions. We study here the behavior of eukaryotic flagellated microswimmers in linear viscosity gradients. Motivated by the near-surface motion of many micro-swimmers, we consider flagellar swimming in two spatial dimensions. We employ a model of flagellum consisting of a semi-flexible filament with a travelling wave of spontaneous curvature to study generic aspects of viscotaxis of actively beating flagella. The propulsion of the flagellum in a fluid due to a hydrodynamic friction anisotropy is described by resistive-force theory. Using numerical simulations and analytical theory, we show that beating flagella exhibit positive viscotaxis, reorienting themselves toward higher viscosity areas. We quantify this behavior by characterization of the dependence of the rotational velocity on gradient strength, beat amplitude, swimming speed, and wave length. We also examine the effects of asymmetric flagellar wave forms, which imply circular trajectories in the absence of viscosity gradients; here, large asymmetry leads to trochoid-like trajectories perpendicular to the gradient in the form of drifting circles. Flagellar deformability strongly reduce the beat amplitude and the viscotatic response. The viscotatic response is shown to be captured by a universal function of the sperm number.

1 Introduction

Sperm cells move in complex environments to find and reach the egg, such as the female reproductive tract for species with internal fertilization, or open water for species with external fertilization, where both eggs and sperm are released into the bulk fluid. This process poses several key challenges for sperm motion: how do sperm steer? How do they change their swimming direction? How do sperm sense and react to different environmental cues? How do environmental patterns such as flow or viscosity gradients influence their trajectory? These are important issues to be clarified in order to understand how sperm can navigate their tortuous journey towards the egg.[1,2]

For an active steering response, two mechanisms have been proposed:[3] an average intrinsic curvature of the flagellum (which leads to a curved or helical trajectory[4,5]) and higher harmonic-beat frequencies.[6] Also, buckling of the flagellum under the load of the propulsion force of the flagellum has been suggested.[7] This steering response can be purposefully employed by the cell for spatial orientation, for example in

Theoretical Physics of Living Matter, Institute for Advanced Simulation and Institute of Biological Information Processing, Forschungszentrum Jülich, 52425 Jülich, Germany. E-mail: s.anand@fz-juelich.de, j.elgeti@fz-juelich.de, g.gompper@fz-juelich.de
† Electronic supplementary information (ESI) available: Model parameters, validation of simulation code, details of analytical calculations, and movie captions. See DOI: https://doi.org/10.1039/d4sm01328j

chemical gradients.[8–11] This chemotactic behavior is typically controlled by biochemical processes in the cell.

In general, the movement of biological microswimmers, such as sperm, can also be significantly influenced by changes in the physical properties of their environment,[12,13] where microswimmers can reorient in external gradients by physical forces exerted on their bodies. Such physical mechanisms – which of course also apply to synthetic microswimmers – include phenomena like rheotaxis,[14–16] where microswimmers can swim upstream in flow through microchannels, and gravitaxis,[17] where they move against the gravitational field.

We focus here on the much less explored effect of viscotaxis, the motion of microswimmers in viscosity gradients. Several recent theoretical and numerical studies[18,19] have demonstrated that various kinds of microswimmers respond to the viscosity gradients, depending on their shape or hydrodynamic propulsion mechanisms. Three-bead model microswimmers have been shown to display positive viscotaxis due to a friction imbalance,[18] while squirmers display negative viscotaxis due to enhanced surface-propulsion forces in high-viscosity fluids.[19,20] Experimental studies of viscotactic behavior have been performed already in the late 1970s for the prokaryotes *Leptospira* and *Spiroplasma*,[21,22] and more recently for the green algae *Chlamydomonas rheinhardtii* using modern microfluidic techniques.[23,24] Significant attention has been paid, both theoretically and experimentally, to the behavior at sharp viscosity changes, as they occurs at soft, penetrable interfaces in binary mixtures of two fluids with different viscosities.[24–26]

In our study, we numerically and theoretically investigate the movement of active eukaryotic flagella, with a snake-like beat pattern, in fluids with spatially varying viscosity. Here, the flagellum is modelled as a semi-flexible filament subject to a traveling bending wave.[27] Our explicit modelling of the beating flagellum allows detailed predictions of viscotaxis in terms of the physical properties of the flagellum, such as bending rigidity of the flagellum, average spontaneous curvature, beat frequency, and wave length, as well as the magnitude of the viscosity gradient.

Here, it is interesting to note that the inherent spontaneous curvature of flagella is an important parameter in sperm navigation. Indeed, sperm cells of various species exhibit a range of morphological shapes, which are often not symmetrical. This asymmetry of some sperm cells facilitates directional steering toward favorable environments, *e.g.* sea urchin sperm have been shown to utilize spontaneous curvature to actively adjust their movement in chemotactic response.[3,28,29]

Sperm often move along surfaces, as their propulsion and hydrodynamic interactions imply an effective, dynamic attraction to surfaces.[30–32] We model this swimming-near-surfaces behavior by considering flagellar motion in two spatial dimensions. Our simulations reveal that individual, symmetrically beating flagella generally exhibit positive viscotaxis, *i.e.* they reorient to align with a viscosity gradient, moving toward regions with higher viscosity. However, asymmetrically beating flagella, with average spontaneous curvature, can swim at finite angles with the gradient or move in drifting circles perpendicular to the gradient direction. These results are valuable for controlling sperm motion in microfluidic devices.[33–37]

2 Model and methods

The sperm flagellum is modelled as an actively beating semi-flexible filament in two dimensions, constructed of N beads connected by bonds to form a linear chain, see Fig. 1(a). The structure and dynamics of the flagellum is described by the position vectors $\mathbf{r}_i$ and velocity vectors $\mathbf{v}_i$ of each bead. The total force $\mathbf{f}_i$ acting on each bead includes the bond force, a curvature-elastic force, and a viscous force due to friction with

the embedding medium. The dynamics of each bead within the flagellum is then governed by the equation of motion

$$\frac{d\mathbf{r}_i}{dt} = \mathbf{v}_i, \quad \frac{d\mathbf{v}_i}{dt} = \frac{\mathbf{f}_i}{m}. \tag{1}$$

Here, a small mass m is used for computational efficiency. Effectively, using a finite mass and velocity allow us to use velocity-Verlet integration, corresponding to using a higher-order integrator with a physically interpretable control parameter, the mass m.[38] However, care has to be taken to reproduce overdamped dynamics, which is achieved by setting mass m and friction coefficient ξ such that the viscous relaxation time m/ξ is much shorter than all other relevant timescales, in particular the beat period τ. We have checked numerically that m/ξ in our simulations is at least by a factor 3 to 5 lower than the threshold value where inertia effects can be detected.

A constant separation between neighboring beads is determined by a harmonic bond potential,

$$U_{\text{bond}} = \frac{k}{2} \sum_{i=0}^{N-1} (|\mathbf{r}_{i+1} - \mathbf{r}_i| - b)^2, \tag{2}$$

where b is the rest length of the spring. To impose a smooth flagellar shape during the beating motion, and a propagating wave in the beat pattern, we employ the bending potential

$$U_{\text{bend}} = \frac{\kappa}{2b^3} \sum_{i=0}^{n-3} (\mathbf{R}_{i+1} - \Re(bC_{\text{flag}})\mathbf{R}_i)^2 \tag{3}$$

where $\mathbf{R}_i$ represents the bond vector that connects two neighbouring monomers, with $\mathbf{R}_i = \mathbf{r}_{i+1} - \mathbf{r}_i$, and κ is the bending rigidity.

The local spontaneous curvature C_{flag} is incorporated by the rotation matrix $\Re(bC_{\text{flag}})$ in eqn (3), which rotates a vector anti-clockwise by an angle of bC_{flag}. A time-dependent local spontaneous curvature[27]

$$C_{\text{flag}}(s,t) = C_0 + A_c \sin(-\omega t + qs) \tag{4}$$

then creates a propagating bending wave along the flagellum, where t is time, and s the position along the flagellum, $\omega = 2\pi/\tau$ (with beat period τ) is the beat frequency, and $q = 2\pi/\lambda$ the beat wave number (with wave length λ). Eqn (4) also contains the curvature amplitude A_c, and a constant average spontaneous curvature C_0 of the flagellum. (Parameters employed in the simulations of this model are collected in Table S1 of the ESI.†)[39]

In previous studies, it was observed that the beating pattern of bull sperm[40] and of human sperm[6] can be well approximated by a single beating mode. Thus, the single mode in eqn (4) captures the essential characteristics of the beat motion.

The bending wave propagates along the flagellum, creating backward fluid motion in the embedding viscous medium, and thereby simultaneously propelling the flagellum forward. We do not model the fluid explicitly in our simulations, but employ resistive force theory (RFT) instead. Here, propulsion is facilitated by the fact that a slender object in a viscous fluid with viscosity η experiences unequal friction coefficients $\xi_\parallel$ and
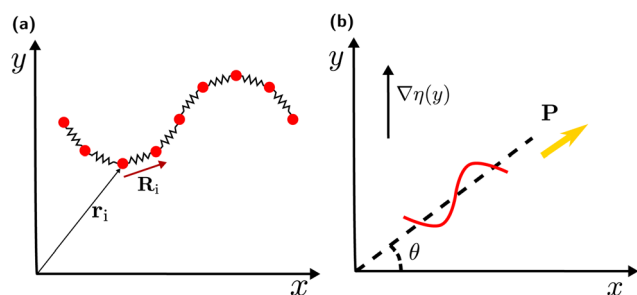
Fig. 1 Model and swimming geometry in a viscosity gradient. (a) Graphical representation of the model for actively beating flagellum, where $\mathbf{r}_i$ is the position vector of particles and $\mathbf{R}_i$ is the bond vector. (b) Schematic of the swimming geometry in a viscosity gradient, with polarity vector $\mathbf{P}$, viscosity-gradient direction $\mathbf{e}_y$, and orientation angle θ, where $\sin(\theta) = \mathbf{P} \cdot \mathbf{e}_y$.

$\xi_\perp$ (both depending linearly on η) for motion tangential and perpendicular to its contour. In the limit of large aspect ratio, the friction anisotropy of a stiff filament is $\xi_\perp/\xi_\parallel = 2$.[41–46] Experimental data for bull sperm[5] yields a somewhat smaller value of $\xi_\perp/\xi_\parallel = 1.81$, which we adopt in our simulations. We apply resistive force theory to each bead in our chain, where the force depends on the local tangent and normal directions of the flagellum, with

$$\mathbf{f}_i^f = -(\xi_\perp \hat{\mathbf{n}}_i\hat{\mathbf{n}}_i^T + \xi_\parallel \hat{\mathbf{t}}_i\hat{\mathbf{t}}_i^T)\mathbf{v}_i, \quad \xi_\perp, \xi_\parallel \sim \eta \tag{5}$$

We employ flagellum length $L = Nb$ and beat period τ as the basic length and time scales in the simulations, respectively. To ensure a realistic representation of sperm flagella, we select parameters that imitate the shape of the natural flagellum beat. A large spring constant kb^2 is employed to keep the bond length nearly constant. To ensure that the dominant deformation is bending rather than stretching, we choose $\kappa/L \ll kb^2$, typically $\kappa/L = 3.18 \times 10^{-4}\ kb^2$. A curvature amplitude $A_cL = 6.28$ generates beat amplitudes A_b of about 15% of the flagellum length L. For more details about the parameter selection in the simulations, see (ESI†),[39] in particular Table S1. Using these parameters, symmetrically beating flagella propel with constant velocity, as expected.

For small enough beat amplitudes, the velocity is well described by[42]

$$v_{\text{flag}} = -\frac{1}{2}\left(\frac{\xi_\perp}{\xi_\parallel} - 1\right)A_b^2\omega q \tag{6}$$

for the beat pattern $y(x,t) = A_b \sin(-\omega t + qx)$, where A_b is the beat amplitude (see ESI† for details[39]). In addition, A_c and A_b are related by $A_b = \lambda^2 A_c/4\pi^2$ for small beat amplitudes.

3 Flagellar motion in viscosity gradients

The main focus of our study is the dynamics of flagellar motion within spatially varying viscosity fields. We model a slowly varying viscosity as a simple linear gradient in viscosity,

$$\eta(y) = \eta_0(1 + \alpha(y - y_{\text{cm}})/L), \quad \xi_\perp, \xi_\parallel \sim \eta(y), \tag{7}$$

where $y_{\text{cm}} = \sum_i m_i y_i \Big/ \sum_i m_i$ represents the y-coordinate of the center of mass. Here, α is the (dimensionless) viscosity gradient coefficient and $\alpha < 1$. The spatial variation in viscosity is small on the scale of flagellum length L.

3.1 Symmetric flagellar beat

3.1.1 Dynamics of flagellar orientation.
To gain insights into the behaviour of a beating flagellum in viscosity gradients, we first consider a flagellum with a symmetric beat, *i.e.* without an average spontaneous curvature, $C_0 = 0$ in eqn (4). Then, symmetry requires that flagella do not rotate without a gradient. The exemplary simulation trajectories in Fig. 2 (see Movie M1, ESI†)[39] show that the flagellum adapts its motion in a viscosity gradient and migrates toward regions of higher viscosity, denoted
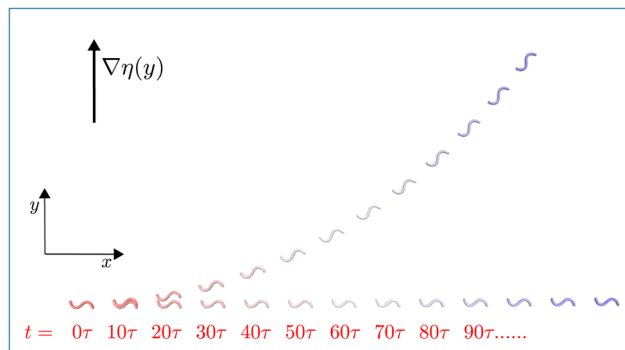

Fig. 2 Flagellum motion in viscosity gradient. Superimposed snapshots of a symmetric beating flagellum under stroboscopic illumination demonstrating the progressive motion of the flagellum in viscosity gradient, with $\alpha = 0.4$, $C_0 = 0$ and $A_cL = 6.28$, compared to the motion without gradient ($\alpha = 0.0$). Snapshot are separated by 10 beat periods τ. See also Movie M1 (ESI†).[39]

as positive viscotaxis. This migration is achieved by reorientation with rotational velocity Ω due to the presence of the gradient.

To quantify the viscotactic behavior, we study the time dependence of the orientation angle $\theta(t)$, which is the angle between the polarity vector (swimming direction) **P** and the positive x-axis, as shown in Fig. 1(b). For a flagellum, which is initiated to swim in the positive x-direction, perpendicular to the gradient, *i.e.* $\theta(0) = 0$, the orientation angle (averaged over the periodic oscillations due to beating) increases roughly linearly in time – until it saturates at $\theta = \pi/2$ for very long times (see Fig. S2(a) in ESI†).[39] We define the rate of reorientation (or angular velocity) $\Omega(\theta,\alpha) = d\theta/dt$. The orientation rate Ω increases with increasing viscosity gradient α (see Fig. S2(b) in ESI†),[39] as expected.

Symmetry dictates that $\Omega(\theta,\alpha)$ must be an odd function in α and a 2π-periodic even function in θ—mirror symmetry to the gradient (sperm facing "left" or "right" of the gradient both rotate towards the gradient) implies $\Omega(\theta) = -\Omega(\pi-\theta)$—hence $\Omega(\theta,\alpha)$ can be expressed as a cosine expansion, *i.e.*,

$$\Omega(\theta,\alpha) = \Omega_1\alpha\cos\theta + \mathcal{O}(\alpha^3), \tag{8}$$

in excellent agreement with simulation results, see Fig. 3. Thus, Ω_1 is the key viscotactic response coefficient. It quantifies how strong the sperm react to a viscosity gradient.

3.2 Viscotaxis mechanism and analytical estimate of reorientation rate

We conjecture that the main underlying mechanism for reorientation in viscotaxis is the drag imbalance of the high- and low-viscosity sides of the swimming flagellum, as illustrated in Fig. 4. This imbalance in forces results in a torque, causing the flagellum to rotate. To calculate this torque analytically, we imagine the beating filament as its sinusoidal shape traveling at constant speed v. This calculation is performed in a body-fixed reference frame, denoted by (x',y'), where the x'-axis is the long axis of the flagellum. In this reference frame, the viscosity gradient appears with a tilt angle θ, which results in a reduced
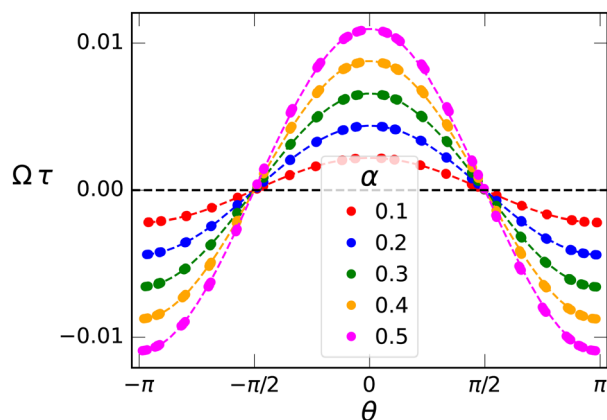
Fig. 3 Quantifying visotactic behavior. Rotational velocity $\Omega(\theta)$ as a function of orientation angle θ for various viscosity gradients α. Solid points are the simulation data, dashed lines are fits to eqn (8). The single fit parameter $\Omega_1\tau = 0.02196$ is the viscotactic response coefficient. Error bars are smaller than the symbol size.
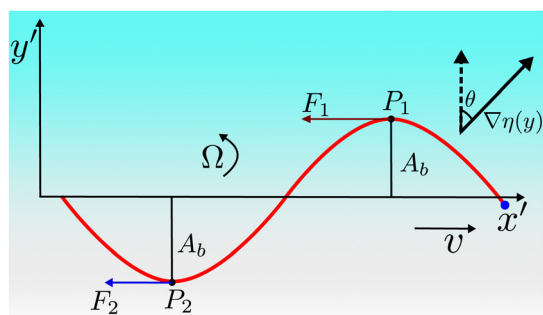

Fig. 4 Swimming in viscosity gradients. Sketch of sperm swimming in viscous gradients in a body-fixed reference frame. The flagellum swims in the x'-direction; the blue small "head" represent the point from which the propagation of the wave takes place. Note that in the body-fixed reference frame, the viscosity-gradient direction appears under an angle θ with respect to the y' axis. P_1 is further up the gradient than P_2, thus F_1 (longer maroon arrow) is larger than F_2 (shorter blue arrow), resulting in a torque toward the gradient.

viscosity difference between the two sides of the flagellum in the body-fixed y'-direction, *i.e.* an effective gradient coefficient $\alpha' = \alpha \cos(\theta)$. The drag forces acting on the flagellum dependent on the local viscosity, and are dominated by $\xi_\parallel$ for small beating amplitudes, as the motion through the fluid is such that the local tangent is essentially always almost parallel to velocity vector and thus to the x'-axis. The torque around the center of mass then reads

$$T_A = \int_{-A_b}^{A_b} y' \bar{\rho}(y') v \xi_\parallel \alpha \cos(\theta) y' \mathrm{d}y' / L \tag{9}$$

with the time-averaged and y-projected mass density of the beating flagellum

$$\bar{\rho}(y') = \frac{1}{\tau}\int_0^\tau \int_0^L \delta(y' - A_b \sin(qx' - \omega t)) \mathrm{d}x' \mathrm{d}t = \frac{L}{\pi}\left(A_b^2 - y'^2\right)^{-1} \tag{10}$$

Combining eqn (9) and (10), we obtain

$$T_A = \frac{1}{2}\alpha \cos(\theta) v \xi_\parallel A_b^2 \tag{11}$$

This torque is balanced by the viscous rotational drag $\xi_{R,F}\Omega$ of the flagellum. For small beat amplitudes, the rotational drag coefficient of the flagellum is approximately equal to that of a rod of the same length, $\xi_{R,rod} = \xi_\perp L^3/12$. It is important to note that as long as the pivot point for the rotation is the geometric midpoint of the flagellum, the rotational drag is not affected by the viscosity gradient, as the increased friction on one half is exactly balanced by the reduced friction on the other half. However, the pivot point shifts toward the higher viscosity side, by a distance proportional to α. Therefore, gradient effects contribute only to the higher-order terms in α, which are not considered here. By generalizing the Gray–Hancock calculation to the case of a viscosity gradient along the flagellar swimming (x') direction, we can also show analytically that gradient contributions cancel out, so that the swimming speed v in eqn (11) is independent of α. Moreover, if the polarity vector **P** (swim direction) is not perpendicular to the gradient, but is inclined at an angle θ, then it is the projection of mass distribution onto the axis perpendicular to the gradient direction $(\nabla\eta)/\eta_0$ which is relevant. The balance of these two torques finally results in (see ESI† for details[39])

$$\Omega = 6\frac{v \xi_\parallel}{L \xi_\perp}\left(\frac{A_b}{L}\right)^2 \alpha \cos(\theta) = 6v\frac{\xi_\parallel}{\xi_\perp}\left(\frac{A_b}{L}\right)^2 \mathbf{P} \times \nabla\left(\frac{\eta}{\eta_0}\right). \tag{12}$$

The approximation of the rotational drag coefficient ξ_R of the flagellum by ξ_{rod} of a stiff rod can be improved for larger beat amplitudes A_b by a correction factor for the rotational drag coefficients $\xi_{R,rod}/\xi_{R,F}$, which is obtained directly from simulations. We calculate the rotational torque for a simulated configuration to obtain an angular velocity Ω, and relate it to the rotational friction as

$$\xi_{R,F} = T_R/\Omega = \left[-\sum_i \mathbf{f}_i \times (\mathbf{r}_i - \mathbf{r}_c)\right]\bigg/\Omega \tag{13}$$

Finally, this is averaged over one beat period, $\langle\xi_{R,F}\rangle_\tau$. The rotational friction coefficient $\xi_{R,F}$ is smaller than $\xi_{R,rod}$, because the beating flagellum is less extended, and some parts have orientational components parallel to the rotational velocity. Thus, for further analysis and quantitative comparison with simulation data, we use a modified form of Ω with an additional factor $\xi_{R,rod}/\xi_{R,F}$, *i.e.*,

$$\Omega = 6\frac{v \xi_{R,rod} \xi_\parallel}{L \xi_{R,F} \xi_\perp}\left(\frac{A_b}{L}\right)^2 \alpha \cos(\theta) \tag{14}$$

This rotational velocity is influenced by three key factors: (i) the magnitude of the viscosity gradient $\alpha \cos(\theta) \propto \nabla\eta$, as already shown above to nicely agree with the simulations, (ii) the beat amplitude A_b, and (iii) *via* the velocity, on the wavelength λ.

In order to test the validity and accuracy of our analytical prediction (14) for Ω, we compare it with simulation data.

We consider first the dependence of Ω_1 on the beat amplitude A_b, while keeping all other parameters constant. Taking into account that the velocity depends quadratically on A_b and inversely on wavelength λ, see eqn (6), the rotational velocity (14) is expected to scale as

$$\Omega_1\tau \sim \omega\tau(A_b/L)^4 L/\lambda. \tag{15}$$

The simulations results (see Fig. 5(a) and Fig. S3 in ESI†)[39] demonstrate that indeed $\Omega \sim A_b{}^4$. Thus, viscotaxis is predicted to display a very pronounced dependence on the beat amplitude.

Fig. 5 illustrates the dependence of the reorientation rate Ω_1 on the flagellar length L. Here, the flagellar length is varied for constant wavelength λ. For $L > \lambda$ ($L < \lambda$) there is more (less) than a single wave on the flagellum. The comparison in Fig. 5(a) demonstrates that there is in general good agreement between the analytical results (14) and simulation for $L > \lambda$. For $L < \lambda$, the observed deviations can be attributed to the assumptions inherent during the derivation of the analytical model; in this regime, the flagellar shape is no longer a travelling sine wave, but rather a short rod-like filament oriented in the swimming direction, which bends left and right periodically. This dependence of Ω_1 on L/λ can be seen more clearly in Fig. 5(b). For $L/\lambda > 1$, the decrease of Ω_1 with increasing L is due to the increasing rotational drag $\xi_{R,F} \propto L^3$, as described by eqn (14). For $L/\lambda < 1$, swimming is impaired due to the absence of a travelling wave, as explained above, so that $\Omega_1 \to 0$ for $L/\lambda \to 0$. This implies that the wave length for optimal viscotasis is $\lambda \simeq L$, as confirmed by the simulation results in Fig. 5(b).

3.3 Asymmetric flagellar beat

3.3.1 Viscotaxis for a flagellum with spontaneous curvature. We model asymmetric beat shapes by introducing a non-zero average spontaneous curvature C_0 in eqn (4). This asymmetry reflects the experimental observation that sperm swim in circles or on helical trajectories[3] in the absence of a viscosity gradient. The spontaneous curvature generates beat patterns that break the symmetry and leads to a non-zero rotational velocity Ω_0 of the flagellum in eqn (8) in the absence of a viscosity gradient, and consequentially to a circular trajectory of the center of mass with clockwise and anti-clockwise motion for $C_0 > 0$ and $C_0 < 0$, respectively.[3] Our analysis focuses on the scenario where the average spontaneous curvature C_0 is constant and does not vary in reaction to environmental conditions.

We examine the effect of beat asymmetry on the viscotactic response. The simulation results in Fig. 6 illustrate that the rotational velocity curve $\Omega(\theta)$ is shifted upwards or downwards for $C_0L < 0$ or $C_0L > 0$, respectively. Therefore, the total rotational velocity Ω can be described as a superposition of the contributions from C_0 and $\nabla\left(\frac{\eta}{\eta_0}\right)$,

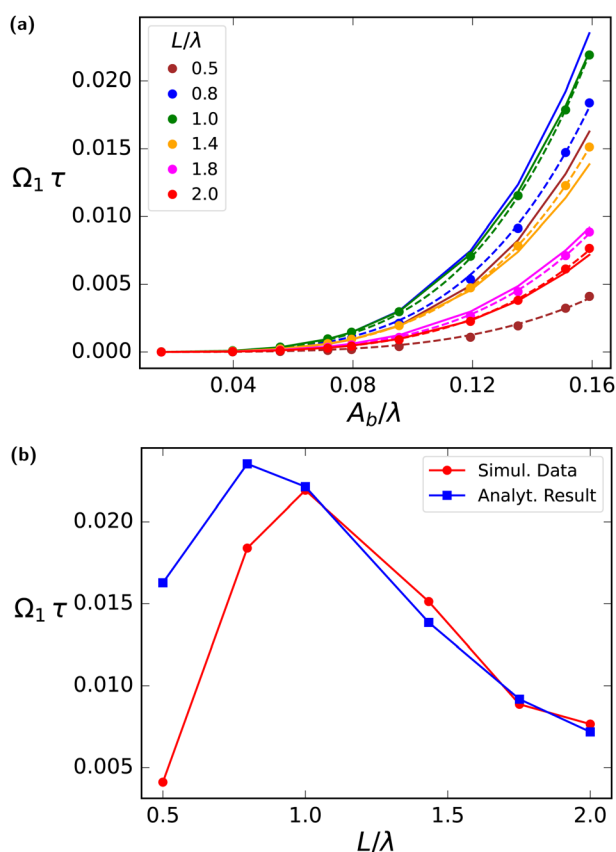$$\Omega = \Omega_0 + \Omega_1\alpha\cos(\theta). \tag{16}$$

Fig. 5 Viscotatic response coefficient Ω_1 as a function of beat amplitude and flagellum length. (a) Rotational velocity $\Omega_1\tau$ as a function of normalised beat amplitude A_b/λ across different flagellum lengths L/λ for simulation (dotted lines) and analytical results (solid lines). The dashed lines are the fit to simulation data. (b) Dependence of rotational velocity $\Omega_1\tau$ on flagellum length L/λ, for a fixed wavelength λ and normalized amplitude $A_b/\lambda = 0.16$, here red solid line with red dot markers represents the simulation data and analytical result is shown by the blue solid line with blue squares markers.
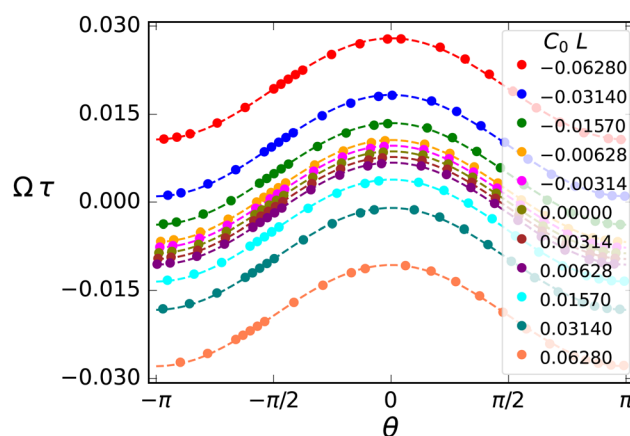

Fig. 6 Rotational velocity with spontaneous curvature. Variation of $\Omega\tau$ as a function of θ for various values of spontaneous curvature, with $\alpha = 0.4$. The peak value, $\Omega(0)\tau$, increases with decreasing $C_0L < 0$ and decreases with increasing $C_0L > 0$.
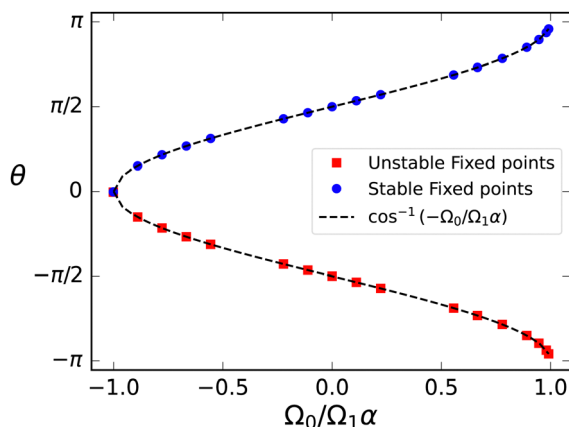
Fig. 7 Stability analysis of fixed points. Variation of the fixed points (θ) as a function of the ratio ($\Omega_0/\Omega_1\alpha$). Stable fixed points from simulation data are indicated by blue circles, while unstable fixed points are represented by red squares. The theoretical prediction given by ($\cos^{-1}(-\Omega_0/\Omega_1\alpha)$) is shown as a black dotted line. The stability of the fixed points changes with ($\Omega_0/\Omega_1\alpha$), highlighting the transition between stable and unstable regimes in the dynamics.

Fig. 8 Phase diagram of trajectory types. Regions of linear and trochoid-like trajectories in a parameter space defined by dimensionless quantities $|\Omega_0|L/v$ and $|\Omega_1\alpha|L/v$. The separatrix $|\Omega_0|/|\Omega_1\alpha| = 1$, as indicated by the black dashed line, separates the two distinct regimes. For $|\Omega_0|/|\Omega_1\alpha| > 1$ the system exhibits trochoid-like[47] motion, while for $|\Omega_0|/|\Omega_1\alpha| < 1$ the system remains stationary.

3.3.2 Phase diagram and stability. The stability analysis of the fixed points of eqn (16) reveals a double saddle-node bifurcation, as shown in Fig. 7. For $|\Omega_0| < |\Omega_1\alpha|$, there are a stable and an unstable fixed point θ^* with $\Omega(\theta^*) = 0$, so that

$$\cos(\theta^*) = -\frac{\Omega_0}{\Omega_1\alpha} \quad (17)$$

at which the flagellar trajectory is asymptotically a straight line. For $\Omega_0 = 0$, the flagellum moves up the gradient at the stable fixed point with $\theta = \pi/2$, while it moves down the gradient at the unstable fixed point with $\theta = -\pi/2$. As spontaneous curvature and Ω_0 decreases ($\Omega_0/(\Omega_1\alpha) \to -1$), both fixed points move towards $\theta = 0$ (bifurcation point). At $\Omega_0 = -\Omega_1\alpha$, the two fixed points meet, resulting in a straight trajectory perpendicular to and to the right of the gradient direction. The second bifurcation happens accordingly in the opposite direction for $\Omega_0/(\Omega_1\alpha) \to +1$. For $|\Omega_0| > |\Omega_1\alpha|$, no fixed point exist, and the flagellum constantly rotates, resulting in a trochoid-like[47] trajectory, as discussed below. With this classification and numerical results, we can construct the phase diagram displayed in Fig. 8.

To illustrate this behavior, we select two curves from Fig. 6, with two spontaneous curvatures $C_0L = -0.0157$ with $\Omega_0 < \Omega_1\alpha$ and two fixed points, and $C_0L = -0.0628$ with ($\Omega_0 > \Omega_1\alpha$) and no fixed point. The corresponding trajectories are shown in Fig. 9. At the stable fixed point, $\cos(\theta^*) = -\Omega_0/\Omega_1\alpha$, the two curvature mechanisms oppose each other, and the flagellum moves on an asymptotically straight trajectory with inclination θ^*. For large Ω_0, the spontaneous curvature dominates, and a trochoid-like trajectory emerges, with drifting circular motion perpendicular to the gradient.

3.3.3 Self-propelled particle model and perpendicular drift. To characterize the trochoid-like drift motion in the phase diagram of Fig. 8 in more detail, we analyze the pitch and the drift direction, which are affected by the viscosity gradient α and spontaneous curvature C_0.
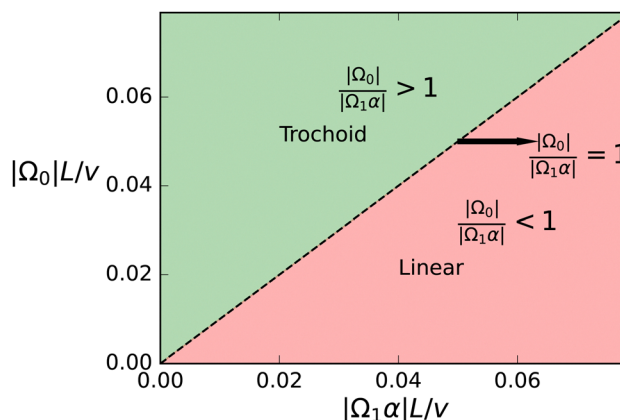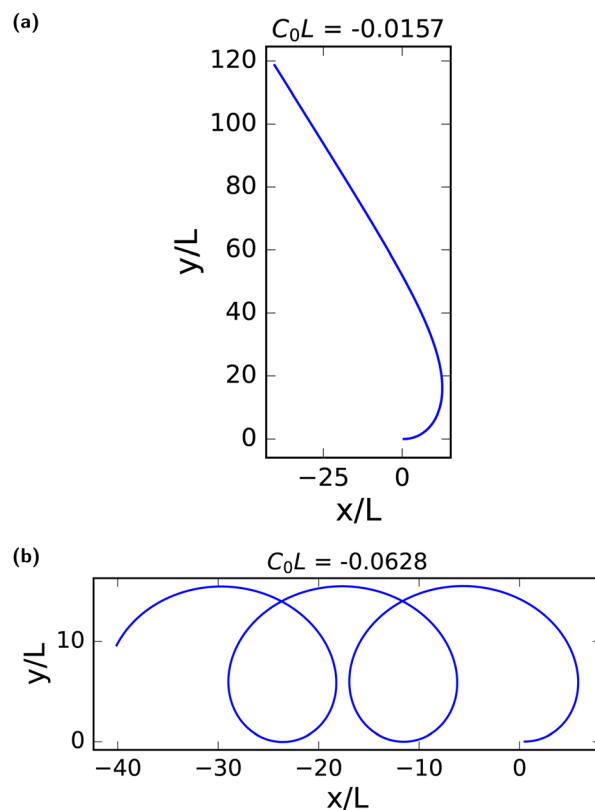

Fig. 9 Trajectory of flagella with spontaneous curvature. Trajectory for the center of mass of beating flagella with average spontaneous curvature (a) $C_0L = -0.0157$ with a stable fixed point, moving on an asymptotically straight trajectory, and (b) $C_0L = -0.0628$ with no fixed point, showing period motion on a trochoid-like[47] trajectory. In both cases, $\alpha = 0.4$. See also Movies M2 and M3 (ESI†).[39]

The dynamics described by eqn (16) is the motion of a self-propelled particle (SPP) in the non-thermal limit, with constant

speed v and a propulsion direction $\mathbf{e}(t)$, which in polar coordinates is $\mathbf{e} = (\cos(\theta), \sin(\theta))$ with inclination angle θ. Under the effect of a redirectional torque, the orientational motion of this particle is governed by

$$\dot{\theta} = \Omega_0 + \Omega_1 \alpha \cos(\theta) \qquad (18)$$

The particle position $\mathbf{r}(t)$ is then obtained from the equation of motion

$$\dot{\mathbf{r}}(t) = v\mathbf{e}(t) \qquad (19)$$

The trochoid-like motion is a periodic motion, compare Fig. 9(b), with time period ΔT. The pitch, denoted as P, defined in analogy with the pitch of a helix, is the distance between two equivalent points on the periodic trajectory along the drift direction. It is calculated over one complete cycle or one time period, from $\theta = 0$ to 2π, i.e.,

$$P = |\Delta \mathbf{r}(t)| = \left| \int_0^{\Delta T} \dot{r}(t) \mathrm{d}t \right| \qquad (20)$$

The time period ΔT of each cycle can be calculated from eqn (18) as

$$\Delta T = \int_0^{2\pi} \mathrm{d}\theta \frac{1}{\Omega_0 + \Omega_1 \alpha \cos(\theta)} = \frac{2\pi}{\sqrt{(\Omega_0)^2 - (\Omega_1 \alpha)^2}} \qquad (21)$$

where $|\Omega_0| > |\Omega_1 \alpha|$. The explicit dependence of $t(\theta)$ on θ is obtained from the indefinite integral of eqn (18) (see ESI† for detail[39]). This shows that increasing Ω_0 reduces the cycle time, while increasing $\Omega_1 \alpha$ extends the cycle time. The cycle time diverges as the fixed point is approached.

To quantify the pitch, we employ perturbation theory, with expansion parameter $\varepsilon = \Omega_1 \alpha / \Omega_0$, which measures the deviation from purely circular motion. Thus, we study the equation

$$\frac{\mathrm{d}\theta}{\mathrm{d}t} = \Omega_0 (1 + \varepsilon \cos(\theta)). \qquad (22)$$

by employing the ansatz $\theta(t) = \theta_0(t) + \varepsilon \theta_1(t)$. For $\varepsilon = 0$, the solution of eqn (22) is $\theta_0(t) = \Omega_0 t$, describing a circular trajectory. The leading-order contribution θ_1 for small ε is then determined by

$$\frac{\mathrm{d}\theta_1}{\mathrm{d}t} = \Omega_0 \cos(\Omega_0 t) \qquad (23)$$

The solution $\theta_1(t) = \sin(\Omega_0 t)$ is used to calculate the translational drift

$$\Delta x = \int_0^{t'} v \cos(\theta_0 + \varepsilon \theta_1) \mathrm{d}t = -v\pi\varepsilon / |\Omega_0| \qquad (24)$$

$$\Delta y = \int_0^{t'} v \sin(\theta_0 + \varepsilon \theta_1) \mathrm{d}t = 0 \qquad (25)$$

where, $\varepsilon = \Omega_1 \alpha / \Omega_0$ and $t' = 2\pi / \left(|\Omega_0| \left(\sqrt{(1 - \varepsilon^2)} \right) \right)$. This results demonstrates two important features of the trochoid-like motion: (i) there is no drift along the y-axis, which shows that
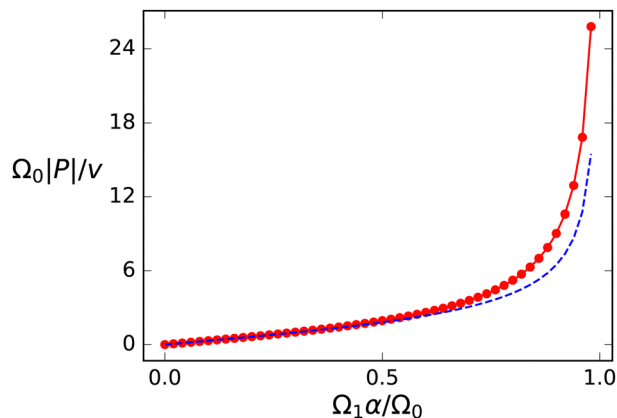

Fig. 10 Pitch P of trochoid-like drift motion. Comparison between theoretical prediction and simulation results for the pitch $\Omega_0 |P|/v$ as a function of the ratio $\Omega_1 \alpha / \Omega_0$. The full red line with markers represents the simulation data, the dashed blue line the theoretical predictions. Good agreement is obtained over the whole accessible range of $\Omega_1 \alpha / \Omega_0$.

the particle always drifts *perpendicular* to the gradient direction, and (ii) the resulting pitch is $P = -v\pi\varepsilon / |\Omega_0| = -\alpha v \pi \Omega_1 / (\Omega_0 |\Omega_0|)$.

Note that the $\alpha \to -\alpha$ inversion symmetry implies that Δx, Δy, and P are odd functions of α. Therefore next-leading terms in eqn (24) and (25), and in the pitch, are of order $\mathcal{O}(\alpha^3)$.

We can generalize this solution for the pitch by combining the first-order perturbation theory with the observation that the pitch must diverge for $\Omega_1 \alpha \to \Omega_0$, and vanishes for $\Omega_1 \alpha = 0$, $\Omega_0 \neq 0$, which results in the approximation

$$P = \frac{-v\Omega_1 \alpha \pi}{\Omega_0 |\Omega_0| \sqrt{1 - (\Omega_1 \alpha / \Omega_0)^2}} \qquad (26)$$

To investigate the quality of this analytical approximation, we compare it with the simulation results, as shown in Fig. 10. The agreement is quite satisfactory over the whole accessible range of $\Omega_1 \alpha / \Omega_0$ values.

3.4 Effect of flagellar elasticity on viscotaxis

A flagellum is not a rigid object, but has a finite elasticity and deformability. The elasto-dynamics of a flexible filament can be conveniently characterized by a single dimensionless parameter, the sperm number Sp,[48,49]

$$\mathrm{Sp}^4 = T_v / \tau = L^4 \xi_\perp \omega / \kappa, \qquad (27)$$

which can be interpreted as the ratio of two-time scales, the beat period $\tau = 2\pi/\omega$ and the typical relaxation time $T_v = 2\pi L^4 \xi_\perp / \kappa$ of an elastic perturbation to propagate along the whole flagellar length L in a viscous environment.

The effect of flagellar deformability has been studied previously for end-actuated flexible filaments[44,49,50] and for trypanosome parasites.[51] However, these cases are more complicated, either due to the highly inhomogeneous wave form, or the large deformable body attached to the flagellum. Some numerical results are also available for sperm.[50]

In order to investigate the dependence of the rotational velocity on the activity-induced deformations of the flagellum,

we study the relation between the rotational velocity Ω_1 and the sperm number Sp by variation of the beat frequency ω for several combinations of bending rigidity κ and perpendicular friction coefficient $\xi_\perp$. In the limit of Sp $\to$ 0, rigidity dominates, and the shape of the flagellum follows exactly the prescribed curvature pattern, whereas at large Sp, viscosity dominates, resulting in additional deformations of the filament.

These additional deformations of the filament change the effective beating amplitude of the flagellum. In order to predict this dependence, we employ the curvature energy for the flexible worm-like filament as a function of its conformation,[52]

$$\mathscr{H} = \frac{\kappa}{2}\int_0^L \left(\partial_x^2 h(x,t) - C_0'(x,t)\right)^2 \mathrm{d}x \qquad (28)$$

for a nearly straight flagellum parallel to the x-axis. Here, $h(x,t)$ represents small perpendicular excursions at a distance x along the filament. $C_0'(x,t)$ denotes the local spontaneous curvature, where a non-zero value means the filament would spontaneously relax to C_0', which is a minimum-energy state. The local spontaneous curvature has the same role as described in eqn (4). We ignore contributions from boundary terms, as they do not influence the subsequent physics. The dynamics of the filament is then governed by the local viscous drag and bending force, derived from eqn (28), and is described by the equation of motion

$$\xi_\perp \frac{\partial h(x,t)}{\partial t} = -\frac{\delta\mathscr{H}}{\delta h(x,t)} = -\kappa\left(\partial_x^4 h - \partial_x^2 C_0'\right) \qquad (29)$$

To solve eqn (29) with a travelling spontaneous-curvature wave, $C_0'(x,t) = \bar{C}_0 e^{i(qx-\omega t)}$, we use a travelling-wave ansatz also for the deflection, $h(x,t) = h_0 e^{i(qx-\omega t)}$, where $h_0 = |h_0|e^{i\phi}$ represents the (complex) beating amplitude. This implies

$$\xi_\perp i\omega h_0 = \kappa(q^4 h_0 + q^2 \bar{C}_0) \qquad (30)$$

$$h_0 = \frac{q^2 \bar{C}_0 L^4}{(i\mathrm{Sp}^4 - q^4 L^4)} \qquad (31)$$

Therefore, the beating amplitude for the beating flagellum is

$$\frac{|h_0|}{L} = \frac{(qL)^2(\bar{C}_0 L)}{\left((qL)^8 + \mathrm{Sp}^8\right)^{\frac{1}{2}}} \qquad (32)$$

Eqn (32) shows that the beating amplitude increases linearly with $\bar{C}_0 L$ and decreases monotonically as a function of Sp^4. In the limit of small sperm number (Sp $\to$ 0), $|h_0|/L = \pi^2\lambda\bar{C}_0 L/4$. A strong decrease of the beat amplitude with increasing Sp, as predicted by eqn (32), is indeed observed in the simulations, see Fig. 11(a). From eqn (31), we can also extract the phase-lag ϕ of the beat wave relative to the spontaneous curvature wave,

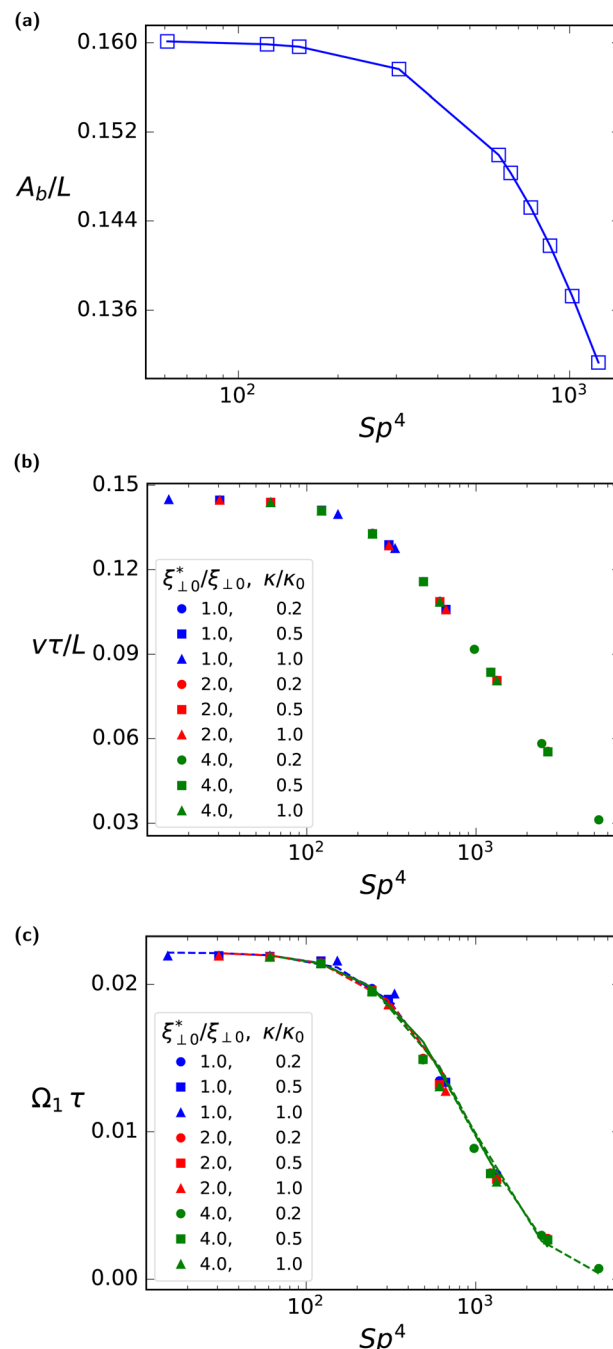$$\sin(\varphi) = \frac{\mathrm{Sp}^4}{\left((qL)^8 + \mathrm{Sp}^8\right)^{\frac{1}{2}}} \qquad (33)$$

Fig. 11 Universal master curves for dependence of beat amplitude, propulsion velocity, and viscotatic response on sperm number Sp^4. (a) Scaled beat amplitude A_b/L of a flagellum for $\alpha = 0.0$, $\xi_{\perp 0}^*/\xi_{\perp 0} = 1.0$ and $\kappa/\kappa_0 = 1.0$. (b) Dimensionless propulsion velocity v/L for $\alpha = 0.0$. (c) Normalized rotational velocity as a function of Sp^4 (with variation of the beat frequency). The dashed lines are the analytical predictions for Ω_1. As the sperm number decreases with decreasing beat frequency, the rotational velocity approaches a plateau. The symbols show simulation data. In (b) and (c), data for different set of parameter pairs $(\xi_\perp, \kappa)$ are displayed.

This implies that $\phi = 0$ for Sp $\to$ 0, i.e. the beat and spontaneous-curvature waves are in phase, while $\varphi = \frac{\pi}{2}$ for Sp $\to$ ∞, i.e. the two waves have the maximum phase shift.

The reduction of beat amplitude with increasing Sp implies a qualitatively similar behavior for the swimming speed, as indicated by the low-amplitude approximation[42] $v \sim A_b^2$, compare eqn (6). This is well confirmed by our simulation results for $\alpha = 0.0$, (Fig. 11(b)), in qualitative agreement with the earlier numerical results for sperm.[50]

Furthermore, the analytical dependence of beating amplitude on Sp^4, eqn (32), can be combined with the swimming speed as a function of Sp^4, to theoretically predict (by employing eqn (14)) the viscotactic response coefficient Ω_1 as a function of Sp^4. The simulation results in Fig. 11(c) show that $\Omega_1\tau$ for various beat frequencies ω and friction coefficients $\xi_\perp$ all fall onto a single master curve, which is described by a universal scaling function Γ, with

$$\Omega_1\tau = \Gamma(\mathrm{Sp}^4). \tag{34}$$

Note that the existence of a master curve already follows from a simple dimensional analysis, as the sperm number Sp is the only dimensionless combination of the parameters ω, κ, $\xi_\perp$, and L.

Moreover, the simulation results closely match the analytical result for the shape of the master curve, see Fig. 11(b). In addition, $\Omega_1\tau$ is found to approach a finite value in the limit $\mathrm{Sp} \to 0$, achieved by decreasing the beat frequency $\omega \to 0$. This is a non-trivial limit, because the rotation frequency vanishes, while the beat period diverges. The fact that the product $\Omega\tau$ remains finite indicates that the rotation of the flagella does not require a dynamic deformation of the flagellum, i.e. the rotational motion is not a consequence of changes in the shape during its beating motion, but due to the friction asymmetry discussed in Section 3.2 above, see eqn (12).

The reduced viscotatic response of the flagellum due to elasticity and deformability is mainly due to a decreasing beat amplitude, which leads to a decreasing friction asymmetry and also a reduced propulsion speed (Gray and Hancock estimate $v/\omega \sim A_b^2$). The combined effect on the viscotactic response is very pronounced due to the strong dependence $\Omega_1 \sim A_b^4$ on the beat amplitude, compare eqn (15). This effect also manifests itself in the angular dependence of the rotation rate $\Omega(\theta)$ in Fig. 12, where the magnitude of Ω decreases both at the minima and maxima – in contrast to the case of spontaneous curvature, where the whole $\Omega(\theta)$ curve shifts upwards. This implies that for elastic flagella, motion perpendicular to the gradient in either direction implies a slower reorientation in the gradient direction due to deformability.

The deformability of the flagellum also affects rotational friction coefficient ξ_R. The results (see Fig. S4 in ESI†)[39] show that $\xi_{R,F}$ increases with increasing flexibility. This contributes to the decrease of Ω_1, because $\Omega_1 \sim 1/\xi_{R,F}$, compare eqn (14). In analogy with the rotational friction of a stiff rod, $\xi_{R,rod} \sim L^3$, we can attribute the increase of $\xi_{R,F}$ to an increment of the projected length, i.e. $\xi_{R,F} \sim L_{eff}^3$, where L_{eff} is end-to-end length of the flagellum due to its deformation. Of course, the increases of the projected length of the flagellum and the decrease of the beat amplitude are geometrically related for fixed contour
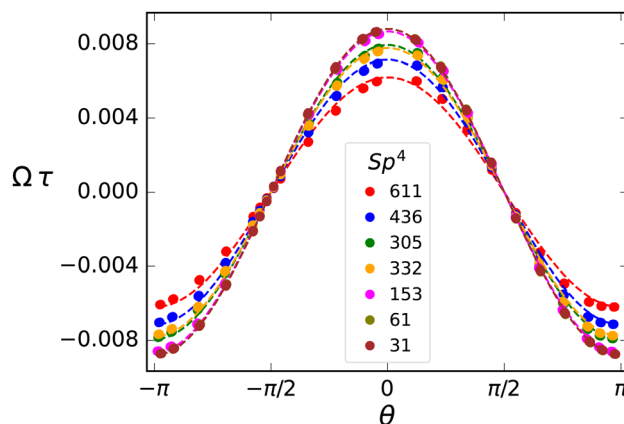

Fig. 12 Rotational velocity *vs.* orientation. Rotational velocity $\Omega\tau$ as a function of orientation θ at different Sp^4 for $C_0L = 0$ and $\alpha = 0.4$.

length of the flagellum, with $L - L_{eff} = \pi^2(A_b/L)^2$ for $\lambda = L$ to leading order in A_b/L (see ESI† for details[39]).

4 Discussion and conclusions

We have studied the viscotactic behavior of flagella by simulating semi-flexible filaments with an active bending wave in two spatial dimensions. Our theoretical and simulation study focuses on the motion of the flagellum in an environment with a linear viscosity gradient. The flagellum is found to reorient toward regions of higher viscosity, where the rotational velocity increases for steeper gradients. We derive an approximate analytical expression for the reorientation rate, which matches our simulation data very well. Additionally, flagella with asymmetric beat determined by an average spontaneous curvature exhibit enhanced viscotaxis. For strong spontaneous curvature, positive viscotaxis is replaced by a trochoid-like drift motion perpendicular to the gradient direction. Flagellar deformability, characterized by the dimensionless sperm number Sp, is found to reduce the beat amplitude, swimming speed, and the viscotactic response.

It is now of course interesting to see which threshold viscosity gradient indices $\alpha^* = \Omega_0/\Omega_1$, which correspond to the boundary between linear (positive viscotaxis) and trochoid (neutral viscotaxis) trajectories in Fig. 8, are predicted for sperm of various species – under the assumption that our flagella results provide reasonable estimates for sperm. Experimental characteristics and resulting estimates are collected in Table 1. These numbers imply the following conclusions and speculations: (i) for circling sperm (bull, sea urchin), the threshold viscosity coefficient α^* is quite large, so that large viscosity gradients are required to induce positive viscotaxis; it is therefore unlikely that viscotaxis plays a significant role in fertilization. In fact, it is known that for sea urchin the circling is intimately connected to the sensing of chemotactic gradients. (ii) In contrast, for human sperm, the threshold viscosity coefficient α^* is small, so that already small viscosity gradients can have a significant effect on guiding the sperm motion.

Table 1 Various experimental characteristics of several sperm species. Typical values for the total length L, swim speed v_0, scaled beat amplitude A_b/L (estimated from the distance between minimum and maximum amplitudes of the beat), scaled intrinsic circling rate $\Omega_0 L/v_0$, scaled viscotactic reorientation rate $\Omega_1 L/v_0$ (calculated from eqn (12)), and threshold viscosity gradient coefficient $\alpha^\star = \Omega_0/\Omega_1$. The medium viscosity is given in units of water viscosity at 20 °C

	$L/\mu m$	$v_0/(\mu m\ s^{-1})$	η/η_w (20 °C)	A_b/L	$\Omega_0 L/v_0$	$\Omega_1 L/v_0$	$\alpha^\star = \Omega_0/\Omega_1$	Ref.
Bull								
In water (36 °C)	60	117	0.7	0.34	1.59	0.385	4.2	5 and 53
In Ficoll 400	60	43	10	0.27	0.84	0.242	3.5	
Sea urchin								
In water	50	200	1.0	0.2	1.5	0.133	11.3	54 and 55
Human								
In water (36 °C)	50	62	0.7	0.13	0–0.05	0.056	0–0.9	7 and 56

Note, however, that human sperm is also spinning around its long axis, which makes the behavior more complex. (iii) It is tempting to speculate that the likely trochoid motion of circling sperm might also play a role in fertilization, as it might prevent positive viscotaxis, and rather make sperm to move "side-wise" in a viscosity gradient, thereby avoiding regions of high viscosity where they may get stuck. In fact, this avoidance effect of high-viscosity regions of trochoid motion may also be an interesting design criterion for microbots.[13]

An important aspect of low-Reynold-number hydrodynamics and overdamped dynamics in a viscous environment is the time reversibility of motion. This may not seem to be the case in viscotaxis – as swimming up-gradient turns in to swimming down-gradient upon time reversal or inversion of swimming direction. However, a closer look reveals that there is no contradiction, as some time is required for flagella to reorient from arbitrary initial condition and to turn up-gradient. Mathematically, this is reflected in the invariance of eqn (8) under time reversal. We denote time-inverted variables with a prime. Under time reversal, velocity is inverted, $i.e.$ $\theta' = \theta + \pi$, and $\Omega' = -\Omega$. Then, it follows from eqn (8) that $-\Omega' = -\Omega_1 \alpha \cos(\theta' - \pi) = -\Omega_1 \alpha \cos(\theta')$, $i.e.$ $\Omega' = \Omega_1 \alpha \cos(\theta')$.

It is important to note that the viscosity gradient and the local viscosity is kept constant in our study. This is of course not possible in a real system, when the flagellum shows positive viscotaxis. In a real system, with constant viscosity gradient $\partial_y \eta$ and initial conditions corresponding to the "positive viscotaxis" region of the phase diagram of Fig. 8, the flagellum moves to regions of higher viscosity, which implies that $\alpha = L(\partial_y \eta)/\eta$ in eqn (12) decreases along the trajectory, until it reaches $\theta = 0$ (or $\theta = \pi$) and moves perpendicular to the gradient. This happens when the separatrix in Fig. 8 – equivalent to the condition $\alpha = |\Omega_0/\Omega_1|$ – is reached. This uniquely determines the asymptotic $y^\star$-position given implicitly through

$$\eta(y^\star) = L(\partial_y \eta)|\Omega_1/\Omega_0|. \tag{35}$$

This implies, in particular, that for deep penetration into a region of higher viscosity, it is advantageous to have a small Ω_0, $i.e.$ a small spontaneous curvature and an nearly symmetrical beat.

This study can be extended in several directions. First, sperm has not only a flagellum but also a head, which adds a frictional load to the flagellar propulsion. This affects the motion in a viscosity gradient in several ways. As the head reduces the beat amplitude in the front part of the flagellum, the amplitude increases from front to tail. Also, pushing the head down-gradient becomes easier than up-gradient (compare ref. 18). Preliminary simulation results show that negative viscotaxis becomes indeed possible in such a case. More studies are required to characterize this behavior in detail. Second, sperm move in the vicinity of surfaces, which is one of the motivation for our modelling in two spatial dimensions. However, motion in two spatial dimensions of course cannot capture all relevant effects of swimming near surfaces, where the head is typically close to the wall and the beating plane can assume various orientations with respect to the wall.[4] Third, most biological fluid are not Newtonian, but often highly viscoelastic. For example shear-thinning could have a significant effect on viscotaxis, as it can modify the local viscosity gradient. Forth, sperm (and many microswimmers) often swim near surfaces, but of course not always. Therefore, it would be very interesting to investigate and characterize the motion in linear viscosity gradients in three dimensions. This case is significantly more complex compared to viscotaxis in two dimensions, as the behavior now depends on the orientation of the beating plane relative to the viscosity-gradient direction. Finally, it would be important to study sperm motion in more complex viscosity landscapes.

Author contributions

G. G. and J. E. designed the research project. S. A. performed the simulations and analysed the obtained data. All authors performed analytic calculations, participated in the discussions and writing of the manuscript.

Data availability

All data are available on zenodo, DOI: **10.5281/zenodo.140 59510**.

Conflicts of interest

There are no conflicts of interest to declare.

Acknowledgements

Notes and references

1 L. Alvarez, B. M. Friedrich, G. Gompper and U. B. Kaupp, *Trends Cell Biol.*, 2014, **24**, 198–207.
2 K. Miki and D. E. Clapham, *Curr. Biol.*, 2013, **23**, 443–452.
3 A. Gong, S. Rode, U. B. Kaupp, G. Gompper, J. Elgeti, B. M. Friedrich and L. Alvarez, *Philos. Trans. R. Soc., B*, 2020, **375**, 20190149.
4 J. Elgeti, U. B. Kaupp and G. Gompper, *Biophys. J.*, 2010, **99**, 1018–1026.
5 B. M. Friedrich, I. H. Riedel-Kruse, J. Howard and F. Jülicher, *J. Exp. Biol.*, 2010, **213**, 1226–1234.
6 G. Saggiorato, L. Alvarez, J. F. Jikeli, U. B. Kaupp, G. Gompper and J. Elgeti, *Nat. Commun.*, 2017, **8**, 1–9.
7 D. J. Smith, E. Gaffney, H. Gadêlha, N. Kapur and J. Kirkman-Brown, *Cytoskeleton*, 2009, **66**, 220–236.
8 M. Yoshida, Y. Hiradate, N. Sensui, J. Cosson and M. Morisawa, *Biol. Bull.*, 2013, **224**, 156–165.
9 J. F. Jikeli, L. Alvarez, B. M. Friedrich, L. G. Wilson, R. Pascal, R. Colin, M. Pichlo, A. Rennhack, C. Brenker and U. B. Kaupp, *Nat. Commun.*, 2015, **6**, 7985.
10 T. Strünker, L. Alvarez and U. Kaupp, *Curr. Opin. Neurobiol.*, 2015, **34**, 110–116.
11 Y. Hong, N. M. Blackman, N. D. Kopp, A. Sen and D. Velegol, *Phys. Rev. Lett.*, 2007, **99**, 178103.
12 J. Elgeti, R. G. Winkler and G. Gompper, *Rep. Prog. Phys.*, 2015, **78**, 056601.
13 G. Gompper, H. A. Stone, C. Kurzthaler, D. Saintillan, F. Peruani, D. A. Fedosov, T. Auth, C. Cottin-Bizonne, C. Ybert, E. Clément, T. Darnige, A. Lindner, R. E. Goldstein, B. Liebchen, J. Binysh, A. Souslov, L. Isa, R. di Leonardo, G. Frangipane, H. Gu, B. J. Nelson, F. Brauns, M. C. Marchetti, F. Cichos, V.-L. Heuthe, C. Bechinger, A. Korman, O. Feinerman, A. Cavagna, I. Giardina, H. Jeckel and K. Drescher, *J. Phys.: Condens. Matter*, 2025, **37**, 143501.
14 A. Zöttl and H. Stark, *Phys. Rev. Lett.*, 2012, **108**, 218104.
15 Marcos, H. Fu, T. Powers and R. Stocker, *Proc. Natl. Acad. Sci. U. S. A.*, 2012, **109**, 4780–4785.
16 K. Qi, H. Annepu, G. Gompper and R. G. Winkler, *Phys. Rev. Res.*, 2020, **2**, 033275.
17 B. ten Hagen, F. Kümmel, R. Wittkowski, D. Takagi, H. Löwen and C. Bechinger, *Nat. Commun.*, 2014, **5**, 4829.
18 B. Liebchen, P. Monderkamp, B. Ten Hagen and H. Löwen, *Phys. Rev. Lett.*, 2018, **120**, 208002.
19 V. A. Shaik and G. J. Elfring, *Phys. Rev. Fluids*, 2021, **6**, 103103.
20 C. Datt and G. J. Elfring, *Phys. Rev. Lett.*, 2019, **123**, 158006.
21 G. Kaiser and R. Doetsch, *Nature*, 1975, **255**, 656.
22 M. J. Daniels, J. M. Longland and J. Gilbart, *J. Gen. Microbiol.*, 1980, **118**, 429–436.
23 M. R. Stehnach, N. Waisbord, D. M. Walkama and J. S. Guasto, *Nat. Phys.*, 2021, **17**, 926–930.
24 S. Coppola and V. Kantsler, *Sci. Rep.*, 2021, **11**, 399.
25 C. Feng, J. J. Molina, M. S. Turner and R. Yamamoto, *Phys. Rev. Res.*, 2022, **4**, 043202.
26 J. Gong, V. A. Shaik and G. J. Elfring, *Sci. Rep.*, 2023, **13**, 596.
27 Y. Yang, J. Elgeti and G. Gompper, *Phys. Rev. E: Stat., Nonlinear, Soft Matter Phys.*, 2008, **78**, 061903.
28 B. M. Friedrich and F. Jülicher, *Proc. Natl. Acad. Sci. U. S. A.*, 2007, **104**, 13256–13261.
29 B. Friedrich and F. Jülicher, *New J. Phys.*, 2008, **10**, 123025.
30 A. P. Berke, L. Turner, H. C. Berg and E. Lauga, *Phys. Rev. Lett.*, 2008, **101**, 038102.
31 J. Elgeti and G. Gompper, *EPL*, 2009, **85**, 38002.
32 J. Elgeti and G. Gompper, *Eur. Phys. J.: Spec. Top.*, 2016, **225**, 2333–2352.
33 V. Kantsler, J. Dunkel, M. Polin and R. E. Goldstein, *Proc. Natl. Acad. Sci. U. S. A.*, 2013, **110**, 1187–1192.
34 P. Denissenko, V. Kantsler, D. J. Smith and J. Kirkman-Brown, *Proc. Natl. Acad. Sci. U. S. A.*, 2012, **109**, 8007–8010.
35 R. Nosrati, P. J. Graham and D. Sinton, *MNF 2014*, 2014, p. 181.
36 R. Nosrati, P. J. Graham, Q. Liu and D. Sinton, *Sci. Rep.*, 2016, **6**, 26669.
37 S. Rode, J. Elgeti and G. Gompper, *New J. Phys.*, 2019, **21**, 013016.
38 R. E. Isele-Holder, J. Jäger, G. Saggiorato, J. Elgeti and G. Gompper, *Soft Matter*, 2016, **12**, 8495–8505.
39 URL_will_be_inserted_by_publisher.
40 I. H. Riedel-Kruse, A. Hilfinger, J. Howard and F. Jülicher, *HFSP J.*, 2007, **1**, 192–208.
41 C. Brennen and H. Winet, *Annu. Rev. Fluid Mech.*, 1977, **9**, 339–398.
42 J. Gray and G. Hancock, *J. Exp. Biol.*, 1955, **32**, 802–814.
43 S. Lighthill, *SIAM Rev.*, 1976, **18**, 161–230.
44 T. S. Yu, E. Lauga and A. Hosoi, *Phys. Fluids*, 2006, **18**, 091701.
45 E. Lauga and T. R. Powers, *Rep. Prog. Phys.*, 2009, **72**, 096601.
46 R. Johnson and C. Brokaw, *Biophys. J.*, 1979, **25**, 113–127.
47 In geometry, a trochoid (from Greek trochos 'wheel') is a roulette curve formed by a circle rolling along a line. It is the curve traced out by a point fixed to a circle (where the point may be on, inside, or outside the circle) as it rolls along a straight line, see https://en.wikipedia.org/wiki/Trochoid.
48 K. Machin, *J. Exp. Biol.*, 1958, **35**, 796–806.
49 E. Lauga, *Phys. Rev. E: Stat., Nonlinear, Soft Matter Phys.*, 2007, **75**, 041916.
50 C. P. Lowe, *Philos. Trans. R. Soc., B*, 2003, **358**, 1543–1550.
51 D. Alizadehrad, T. Krüger, M. Engstler and H. Stark, *PLoS Comput. Biol.*, 2015, **11**, e1003967.
52 M. Doi and S. F. Edwards, *The Theory of Polymer Dynamics*, Clarendon Press, Oxford, 1986.

53 R. Rikmenspoel, *J. Exp. Biol.*, 1984, **108**, 205–230.
54 M. Böhmer, Q. Van, I. Weyand, V. Hagen, M. Beyermann, M. Matsumoto, M. Hoshi, E. Hildebrand and U. B. Kaupp, *EMBO J.*, 2005, **24**, 2741–2752.
55 D. Woolley and G. Vernon, *J. Exp. Biol.*, 2001, **204**, 1333–1345.
56 J. A. Mossman, J. T. Pearson, H. D. Moore and A. A. Pacey, *Hum. Reprod.*, 2013, **28**, 22–32.